Article

Implementation of Nonlinear Controller to Improve DC Microgrid Stability: A Comparative Analysis of Sliding Mode Control Variants

Syeda Shafia Zehra *[ID], Alberto Dolara [ID], Muhammad Ahsan Amjed [ID] and Marco Mussetta [ID]

Department of Energy, Politecnico di Milano, 20156 Milano, Italy; alberto.dolara@polimi.it (A.D.);
muhammadahsan.amjed@polimi.it (M.A.A.); marco.mussetta@polimi.it (M.M.)
* Correspondence: syedashafia.zehra@polimi.it

Abstract: Electricity generation from sustainable renewable energy sources is constantly accelerating due to a rapid increase in demand from consumers. This requires an effective energy management and control system to fulfil the power demand without compromising the system's performance. For this application, a nonlinear barrier sliding mode controller (BSMC) for a microgrid formed with PV, a fuel cell and an energy storage system comprising a battery and supercapacitor working in grid-connected mode is implemented. The advantages of the BSMC are twofold: The sliding surface oscillates in the close vicinity of zero by adapting an optimal gain value to ensure the smooth tracking of power to its references without overestimating the gains. Secondly, it exhibits a noticeable robustness to variations and disturbance, which is the bottleneck of the problem in a grid-connected mode. The stability of the presented controllers was analyzed with the Lyapunov stability criterion. Moreover, a comparison of the BSMC with sliding mode and supertwisting sliding mode controllers was carried out in MATLAB/Simulink (2020b) with real PV experimental data. The results and the numerical analysis verify the effectiveness of the BSMC in regulating the DC bus voltage in the presence of an external disturbance under varying conventional load and environmental conditions.

Keywords: adaptive gain; barrier sliding mode control; energy storage system; microgrid; nonlinear controller

1. Introduction

As the energy demand is constantly on the rise, the generation of electricity from fossil fuels has also increased, which has resulted in an alarming elevation in CO_2 emissions [1]. The ongoing energy crisis has prompted researchers to consider multiple options for electricity generation. A greener and more effective solution for electricity production is from renewable energy sources (RESs), which mainly include solar, wind, hydro and tidal energies [2]. Solar energy is abundant in nature and is predicted to meet 95% of the energy demand by 2026 [3]. Since the RESs exhibit a stochastic nature in terms of energy production, they need suitable forecasting tools to be managed [4], and they are accompanied by energy storage systems to guarantee an adequate power supply under all conditions [5]. Among them, batteries and supercapacitors (SCs) are proven to be the most reliable energy storage units due to their promising characteristics [6].

In the past few years, the utilization of fuel cells (FCs) has proved to be a feasible alternative for the production of clean energy. The proton exchange membrane fuel cell (PEMFC) has been applied in electric vehicles and large-scale grids depending on the power demand. To generate power, the PEMFC is provided with either hydrogen or compounds of hydrocarbons, which can later decompose to supply hydrogen. FCs are characterized based on their electrolytes, such as solid oxide FCs, molten carbonate FCs, phosphoric acid FCs and alkaline FCs, which have different operating temperatures and power capacities. They

can deliver variable power depending on the application, ranging from 0.2 kW (unmanned aerial vehicles) to 1 MW (trains and tramways) [7].

One of the major drawbacks of FCs is their short lifespan, which is a barrier to implementing them as a reliable energy source in large-scale applications [8]. To ensure power availability and smooth operation under varying load conditions, it is necessary to integrate proper load forecasting approaches and additional energy storage sources [9,10]. Owing to their remarkable characteristics, batteries and SCs are the most suitable energy storage devices as an auxiliary source in a system, along with FCs, increasing lifespan as well as quickly dealing with high power transients [11]. The main power source typically has high energy density, so it operates during low load demand and is responsible for keeping the energy storage devices charged over time. Moreover, SCs exhibit high power density, which makes them a reliable energy source during high power fluctuations, whereas batteries known for their high energy density, so they are used as a hybrid energy storage system (HESS) with FCs [12].

To obtain maximum power from the FC and HESS, a wide range of research has been carried out over time on their integration of DC–DC converters. Boost, buck and buck–boost are the most commonly utilized converter topologies and are capable of stepping up or down the output voltage [13]. Additionally, work has been carried out on the converter topologies and the selection of components that play an important role in fulfilling the load demand without compromising the performance of the system [14]. The selection of capacitor and inductor values holds great importance as it directly affects the performance of the DC–DC converters [15]. H_∞ control has been employed in one of the approaches to controlling the output from a DC–DC interleaved boost converter [16]. The goal is to have minimum ripples and harmonics in the current to increase the lifetime of the FC and HESS, for which a smaller component size is preferred [17]. Moreover, to include all the dynamics of the DC–DC converters in the simulation, an average state-space model is generally considered.

The microgrid's goal is optimized when its subsystems are closely coordinated and organized. This necessitates an integrated framework that enables each subsystem to function autonomously while fostering effective intercommunication. This objective is achieved by implementing a system-of-systems (SoS) framework, which comprehensively handles the management, communication and control requirements of the microgrid systematically [18]. The design of the controller in an SoS approach is an essential task after designing the DC–DC converters as it plays a crucial role in the DC bus voltage regulation. Various control designs have been investigated in the literature, including the implementation of proportional–integral (PI) controllers in electric vehicles and grids to guarantee adequate energy management [19,20]. A PI controller works best when its operating point is linearized, but its performance is compromised in the presence of disturbances [21]. Similarly, other control techniques including droop control [22], feedback linearization and robust H_∞ control have also been implemented to control the output from energy storage devices which fail to achieve global consistency, leading to compromised performance [23,24]. The integration of various renewable energy sources along with hybrid energy storage units gives rise to several non-linearities, which include chaotic behavior in their system and non-minimal phase behavior, which results from the lagging of the inductor current and dynamic changes due to the switching of DC–DC converters. Considering the aforementioned factors, nonlinear controllers exhibit better performance in such scenarios over PI controllers presented in previous works [25]. Moreover, the linear controllers perform better only in their local region, and nonlinear controllers are taken into account to ensure the global stability of the system as well [26]. Various nonlinear controllers have been presented for the control of energy storage systems, of which the backstepping controller, Lyapunov redesign and sliding mode controller (SMC) are widely used [27]. A comparison between integral backstepping control and the SMC has been presented, which shows better performance of the nonlinear SMC in the case of autonomous systems [28]. An economic analysis for electric vehicles employing a HESS with nonlinear

control has been presented, stating the reduction in fuel consumption with STSMC [29]. The favorable characteristics of the SMC, i.e., its robustness to disturbances and uncertainties along with its simple design, make it the foremost option for dealing with state-space model based systems [30].

Controllers based on the higher-order SMC are widely implemented for controlling the output voltage from DC–DC converters for charging electric vehicles, in DC microgrids [31] and in advanced aeronautic applications [32,33]. Integral and double integral SMCs have been implemented to minimize the error between the references and the desired signals [34]. Adaptive and adaptive terminal SMCs have also gained significant attention due to the ease with which the gains can be adjusted automatically to maintain the error close to zero [28]. On the other hand, it is pertinent to mention a phenomenon called chattering displayed by SMCs, which results in undesirable oscillations in the output signals [35]. To minimize this, several approaches have been presented, of which super-twisting sliding mode control (STSMC) is the most renowned [36,37]. This technique has been applied to single-input single-output systems as well as multi-input multi-output systems, grid-connected power systems and a buck converter connected to a constant power load [38].

To design a robust nonlinear controller that possesses the characteristics absent in the previous works, i.e., dealing with uncertainties and disturbances without exceeding the controller gain boundary values, a barrier function dependent sliding mode controller (BSMC) [39] has been implemented in this work to control the output power from PV, the FC, the battery and the SC through the connected DC–DC converters working in a grid-connected mode to fulfil the load demand from the conventional load in the presence of disturbance and uncertainties. The schematic of the system under study is presented in Figure 1. As the PV system supplies intermittent power, the FC is considered the main source with the battery and SC acting as the auxiliary sources.
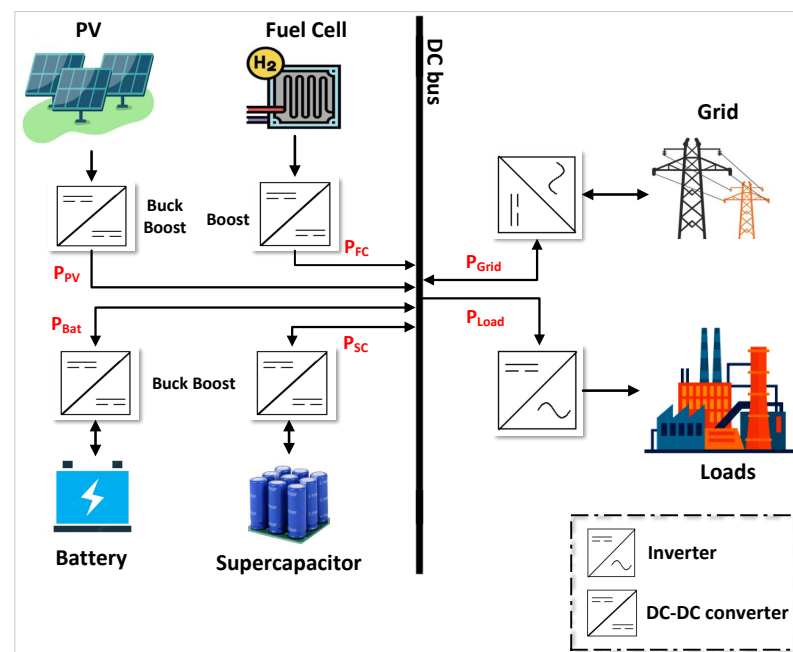

Figure 1. Proposed structure of embedded power sources in the microgrid: PV–FC–battery–SC.

The main contributions of this work in implementing the aforementioned design are highlighted as follows:

- The implemented BSMC combines an adaptive barrier function gain to ensure that the state trajectories remain within close vicinity of zero. This reduces the error without overestimating the controller gains as referred to in the literature review.
- The robustness of the controller has been tested in the presence of an external disturbance to ensure its effectiveness in the primary control level of the SoS framework.

- A comparison between the SMC, supertwisting SMC and barrier-based SMC has been carried out to show the effective performance of the latter controller without increasing the gains of the controller.

To sum up, this paper is structured as follows: Section 2 explains the objectives and model of the system, and the connection of the sources with the DC–DC converters are discussed. Section 3 outlines the design of the sliding mode and the derivation of the nonlinear barrier sliding mode controllers for PV and the HESS in detail along with the adaptive gain adjustment. Section 4 presents the findings of this approach through MAT-LAB/Simulink and displays the results of the controller's performance. Section 5 details the performance of the BSMC with the real experimental PV profile and its comparison with SMC and STSMC control variants, and lastly Section 6 concludes the paper with a brief overview along with the findings and some future prospects of this work.

2. System Design and Objectives

The presented system generates power from a PV source operating at its maximum power point along with the FC operating as the primary source supplying power during low power demand. Illustrated in Figure 1, the output from PV is controlled with a DC–DC buck–boost converter capable of stepping up or down the output voltage according to the power absorbed by the conventional load. The battery and SC work together as the supplementary sources charging and discharging accordingly, i.e., absorbing or providing power. To regulate the DC bus voltage, the FC is connected to a boost converter to step up the output voltage, and the battery and SC are interfaced with buck–boost converters for the bi-directional flow of currents to allow their charging and discharging. Presented in Figure 2 is the rule-based energy management algorithm adopted in this framework to generate the power references for the BSMC [40]. It is the secondary-level control in an SoS framework responsible for generating the power references to be tracked by the primary-level controller. This approach employs fuzzy-logic rule-based EMS which takes input power from the converters and generates the output reference power for the FC and hybrid energy storage system, according to the designed rules.

The state-space model for this system can be expressed as follows [41,42]:

$$\frac{dV_{PV_i}}{dt} = \frac{I_{PV}}{C_{pv1}} - \frac{I_{L_{PV}}}{C_{pv1}} u_1 \tag{1}$$

$$\frac{dI_{L_{PV}}}{dt} = \frac{V_{C_{pv1}}}{L_{PV}} u_1 - \frac{V_{C_{pv2}}}{L_{PV}} (1 - u_1) \tag{2}$$

$$\frac{dV_{PV_o}}{dt} = \frac{I_{L_{PV}}}{C_{pv2}} (1 - u_1) - \frac{I_{PV}}{C_{pv2}} \tag{3}$$

$$\frac{dI_{FC}}{dt} = \frac{-R_{FC}}{L_{FC}} I_{FC} + \frac{1}{L_{FC}} V_{FC} - \frac{1 - u_2}{L_{FC}} V_{DC} \tag{4}$$

$$\frac{dI_{Bat}}{dt} = \frac{-R_B}{L_B} I_{Bat} + \frac{1}{L_B} V_{Bat} - \frac{u_{34}}{L_B} V_{DC} \tag{5}$$

$$\frac{dI_{SC}}{dt} = \frac{-R_{SC}}{L_{SC}} I_{SC} + \frac{1}{L_{SC}} V_{SC} - \frac{u_{56}}{L_{SC}} V_{DC} \tag{6}$$

$$\frac{dV_{DC}}{dt} = \frac{1 - u_2}{C_o} I_{FC} + \frac{u_{34}}{C_o} I_{Bat} + \frac{u_{56}}{C_o} I_{SC} - \frac{1}{C_o} i_o \tag{7}$$

In the model presented from Equations (1)–(7), R_{FC}, R_B, R_{SC}, L_{PV}, L_{FC}, L_B, L_{SC}, C_{pv1}, C_{pv2} and C_o are the resistors, inductors and capacitors connected to the DC–DC converters to control the output from the power sources. u_1, u_2, u_{34} and u_{56} are the control signals generated by the BSMC and are provided as inputs to the switches of the DC–DC converters. The designed BSMC tracks the power references provided by the higher-level energy management systems (EMSs) based on artificial intelligence algorithms. The parameters of the DC–DC converters are known, and the BSMC-based control signals u_i

are derived for DC–DC converter switches of the power sources whose specifications are given in Table 1.
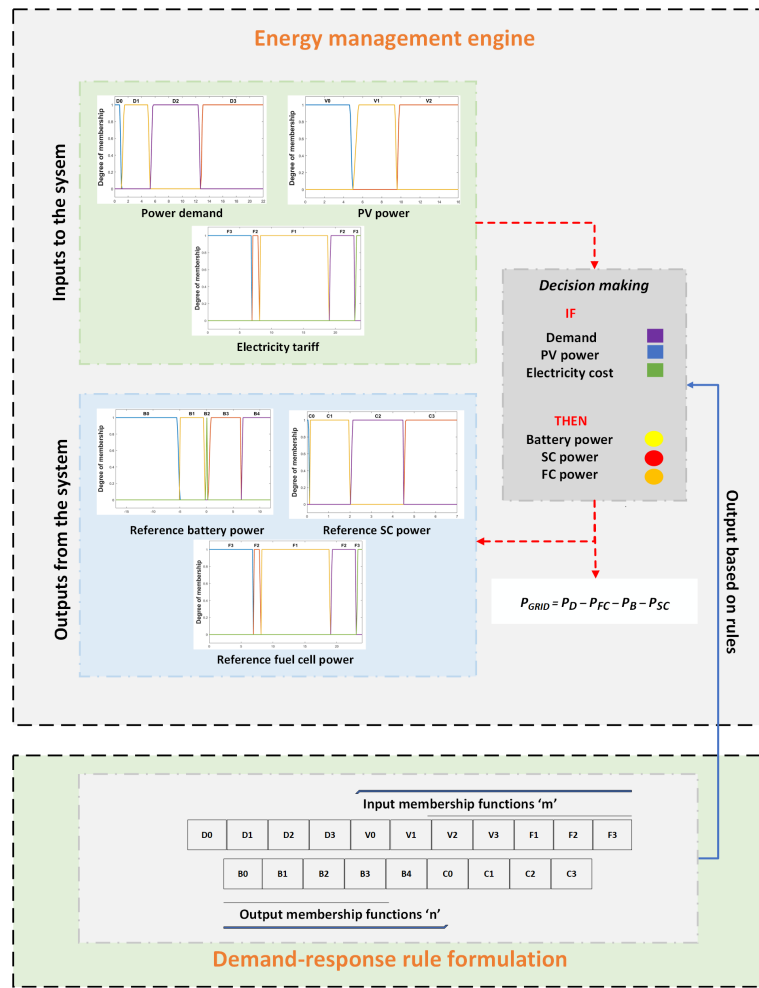

Figure 2. Energy management of power sources using artificial-intelligence-based algorithm.

To simplify the aforementioned model for the derivation of the controller, the terms V_{PV_i}, $I_{L_{PV}}$, V_{PV_o}, I_{FC}, I_{Bat}, I_{SC} and V_{DC} have been rewritten as y_1, y_2, y_3, y_4, y_5, y_6 and y_7, respectively. The obtained state-space model can be written as follows:

$$\frac{dy_1}{dt} = \frac{1}{C_{pv1}}I_{PV} - \frac{u_1}{C_{pv1}}y_2 \tag{8}$$

$$\frac{dy_2}{dt} = \frac{u_1}{L_{PV}}y_1 + \frac{u_1}{L_{PV}}y_3 - \frac{1}{L_{PV}}y_3 \tag{9}$$

$$\frac{dy_3}{dt} = \frac{1-u_1}{C_{pv2}}y_2 - \frac{1}{C_{pv2}}I_{PV} \tag{10}$$

$$\frac{dy_4}{dt} = \frac{1}{L_{FC}}V_{FC} - \frac{R_{FC}}{L_{FC}}y_4 - \frac{1-u_2}{L_{FC}}y_7 \tag{11}$$

$$\frac{dy_5}{dt} = \frac{1}{L_B}V_{Bat} - \frac{R_B}{L_B}y_5 - \frac{u_{34}}{L_B}y_7 \tag{12}$$

$$\frac{dy_6}{dt} = \frac{1}{L_{SC}}V_{SC} - \frac{R_{SC}}{L_{SC}}y_6 - \frac{u_{56}}{L_{SC}}y_7 \tag{13}$$

$$\frac{dy_7}{dt} = \frac{1-u_2}{C_o}y_4 + \frac{u_{34}}{C_o}y_5 + \frac{u_{56}}{C_o}y_6 - \frac{1}{C_o}i_o \tag{14}$$

After defining the model of the system, the objectives of this work were defined as:

1. To minimize the effect of chattering by analyzing and selecting the suitable controller parameters,
2. To ensure the tracking of the FC, battery and SC power to their references provided by the energy management algorithm,
3. To ensure that the system shows robustness to uncertainties and disturbances with improved dynamic performance,
4. To meet the power demand throughout the charging and discharging periods of the HESS,
5. To ensure the DC bus voltage regulation in all scenarios, i.e., absorbing power from the grid or supplying power to the grid.

Table 1. Specifications of the power sources.

Model of PV Array	
Parallel connected strings	1
PV module per string	10
Number of cells per module	60
Short circuit current	7.84 A
Open circuit voltage	363 V
Current @MPP	7.35 A
Voltage @MPP	290 V
Module's maximum power	2.1 kW
Model of Fuel Cell	
Nominal current	250 A
Nominal voltage	350 V
Maximum power	34 kW
Model of Lithium-Ion Battery Module	
Rated capacity	4.4 Ah
Rated voltage	115 V
Number of cells	32
Power	15 kW
Specific power	1071.4 W/kg
Weight	14 kg
Specific energy	36.14 Wh/kg
Dimensions (L × W × H)	417 × 304 × 135 mm
Model of Supercapacitor	
Rated capacitance	165 F
Rated voltage	48 V
Number of cells	18
Maximum ESR	6.3 mΩ
Capacitance of individual cells	3000 F
Absolute maximum current	1900 A
Typical mass	13.5 kg
Specific energy	3.9 Wh/kg
Usable specific power	3300 W/kg
Dimensions (L × W × H)	418 × 194 × 126 mm

3. Implementation of Nonlinear Barrier Sliding Mode Controller

A barrier sliding mode controller (BSMC) was designed and implemented for the control of energy generation units. As stated in the objectives, this controller incorporates parameters which make it robust towards disturbances. The performance exhibited by the BSMC can be explained in the following fashion: When the sliding surface is in the predefined boundary of error, it behaves as an SMC with a constant gain. Contrarily, when the sliding surface is outside the predefined boundary, the BSMC adjusts its gain to bring the sliding surface back into the defined range to ensure the convergence of error to zero.

In this way, the chattering displayed by the SMC minimizes due to the adaptive adjusting of the sliding surface gain by the BSMC.

To demonstrate the working of this system, an overall design is presented in Figure 3. The currents and voltages from the respective DC–DC converters are delivered to the controllers to generate the control signals u_1, u_2, u_{34} and u_{56} according to the reference power provided by the EMS. Furthermore, these control signals generate the required power from the converters by controlling the switching, hence forming a closed loop. In the derivation of nonlinear controllers, the Lyapunov stability criterion is always fulfilled to maintain the closed-loop system stability. The sliding surface S ensures that the derivative of the Lyapunov function is always negative, which ensures the stability of the system [39]. The first step in the design of the SMC is defining a sliding surface as follows [37]:

$$S_i = m_i e_i \tag{15}$$

$$e_i = y_i - y_{iref} \tag{16}$$

Equation (15) gives a general representation of a sliding surface in which the term m is the constant of the sliding surface in charge of minimizing the tracking error defined in Equation (16). y_i represents the state currents to be tracked to their references y_{iref} provided to the controller by the energy management system shown in Figure 2. To hold the sliding surface in the close neighborhood of zero, four sliding surfaces $S_{i=1,...,4}$ are defined in this section for the derivation of control signals. For the convergence of errors to zero, their sliding surfaces must converge to zero with time as well. The time derivative of the sliding surface can be expressed as:

$$\dot{S}_i = m_i \dot{e}_i \tag{17}$$

Replacing the derivative of error $\dot{e}_i$ in Equation (17) with its derivative from Equation (16) and equating it with the following reaching law expression for SMC:

$$-a_i \left| S_i \right|^{\alpha_i} sign \left(\frac{S_i}{\rho_i} \right) = m_i (\dot{y}_i - \dot{y}_{iref}) \tag{18}$$

This concept is referred to as the power-rate reaching law, which enhances the rate of convergence as the state moves farther from the switching manifold. The term $Sign(S_i)$ in Equation (18) represents the signum function, which switches between -1, 0 and 1 according to the movement of the sliding surface and is defined as [39]:

$$Sign\left(S_i\right) = \begin{cases} -1 & if \ \ S_i < 0 \\ 0 & if \ \ S_i = 0 \\ 1 & if \ \ S_i > 0 \end{cases} \tag{19}$$

In Equation (18), ρ_i and α_i are the design parameters of the controllers, which are fixed between 0 and 1 to reduce the chattering and to guarantee the convergence of errors to zero [37]. a_i is the controller gain, which differs the BSMC from the SMC and STSMC since it behaves as a constant gain in the SMC and STSMC, while it behaves as an adaptive gain of the barrier function in the BSMC, which continues to switch between its defined barrier depending on the sliding surface's trajectory. The value of the adaptive gain increases until the sliding surface reaches a small neighborhood of zero ε by employing a positive constant gain $\bar{a}$. ε is the controlling parameter for the adaptive gain of the barrier function and sliding surface. The value of ε is kept very small, i.e., close to zero, to keep its dependents closer to zero as well. In the presence of a disturbance, when the trajectory of the sliding surface deviates away from zero, the value of the adaptive gain increases. On the other hand, the adaptive gain decreases along with the sliding surface when there is a decaying disturbance, ensuring that the sliding surface is always approaching zero. Large disturbances in uncertain systems lead the system to instability as the controller gain tends to increase, leading to an increase in chattering amplitude, i.e., in the case of the sliding mode controller (SMC) [43] and supertwisting sliding mode controller (STSMC) [44]. In

the case of the BSMC, it adopts an adaptive strategy that can achieve the convergence of the output variable to a predefined neighborhood of zero, with a controlled gain that is not overestimated and without using any information about the upper bound of the disturbance. Consequently, the gain of the controller stays within the predefined boundary and cannot exceed it for any disturbance. The behavior of the adaptive gain concerning time can be mathematically expressed as [39]:

$$a_i(t, S_i(t)) = \begin{cases} a_i(t), \dot{a}_i(t) = \bar{a}_i |S_i(t)| & if \ 0 \leqslant t \leqslant \bar{t} \\ a_i(S_i(t)) & if \ t > \bar{t} \end{cases} \tag{20}$$

$$a_i(S_i(t)) = \frac{|S_i|}{\varepsilon - |S_i|} \tag{21}$$

Initially, the controller gain a_i is increased by tuning until the state trajectories reach the close neighbourhood of zero, defined in this paper as ϵ, of the SMC surface $S(t)$ at time $\bar{t}$ given in Equation (20). For the times after $\bar{t}$, the adaptive gain a_i switches to the barrier function, which decreases the convergence region and maintains the state trajectories. The sliding surface gains m_i arbitrary positive constants selected to be very small as the derivative of the sliding surface is a product of this gain and the derivative of the error between the references and the state trajectories stated by Equation (15) [45].
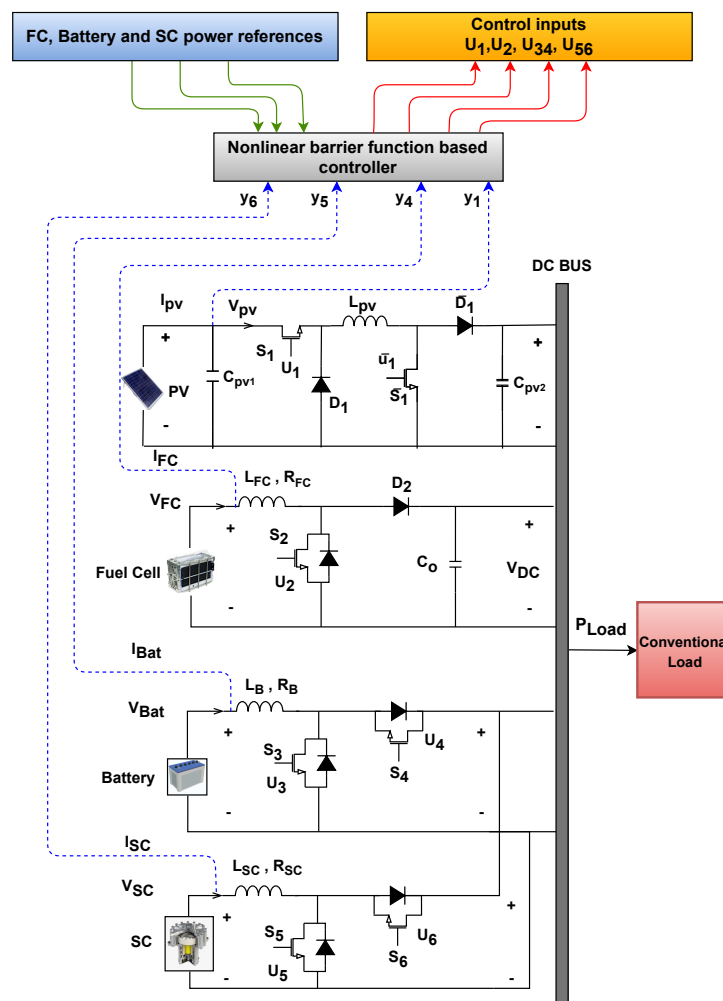

Figure 3. In-loop presentation of proposed control strategy with power references generated from AI-based energy management system.

The STSMC has also been implemented for the control of distributed energy units in microgrids; however, its performance is compromised in the presence of disturbance due to a nonlinear term existing in its control law [44]. The basic difference between the BSMC and STSMC can be expressed in terms of its control law formulation, which is designed as follows:

$$\dot{S}_i = -a_i \, |S_i|^{\alpha_i} \, sign \left(\frac{S_i}{\rho_i} \right) - a_k \int sign \left(\frac{S_i}{\rho_i} \right) dt \qquad (22)$$

In Equation (22), a_i and a_k represent the STSMC gains with positive constant values compared to the BSMC with an adaptive gain. To derive a BSMC u_1 for the PV array, the first step as defined earlier is the formation of a sliding surface based on its error as follows:

$$S_1 = m_1 e_1 \qquad (23)$$

To operate the PV array at its maximum power point, the BSMC should track its voltage y_1 to its desired reference y_{1ref}. For this purpose, the error term has been modeled as shown:

$$e_1 = y_1 - y_{1ref} \qquad (24)$$

The time derivative of the sliding surface given in Equation (23) can be formulated as:

$$\dot{S}_1 = m_1 \dot{e}_1 \qquad (25)$$

To solve Equation (25), the time derivative of the error given in Equation (24) can be modeled as:

$$\dot{e}_1 = \dot{y}_1 - \dot{y}_{1ref} \qquad (26)$$

Replacing the value of $\dot{y}_1$ from Equation (8) in Equation (26) yields the following expression:

$$\dot{e}_1 = \frac{I_{PV}}{C_{pv1}} - \frac{u_1}{C_{pv1}} y_2 - \dot{y}_{1ref} \qquad (27)$$

To finally analyze the expression for the derivative of the sliding surface, $\dot{e}_1$ has been substituted from Equation (27) in Equation (25):

$$\dot{S}_1 = m_1 \left[\frac{I_{PV}}{C_{pv1}} - \frac{y_2}{C_{pv1}} u_1 - \dot{y}_{1ref} \right] \qquad (28)$$

To facilitate the convergence of error to zero, $\dot{S}_1$ has been replaced with the following expression given in Equation (18):

$$\dot{S}_1 = -a_1 \, |S_1|^{\alpha} \, sign \, (\frac{S_1}{\rho_1}) \qquad (29)$$

where the adaptive barrier function gain a_1 for the sliding surface S_1 is defined in Equation (20). Equating Equations (28) and (29) results in:

$$-a_1 \, |S_1|^{\alpha_1} \, sign \, (\frac{S_1}{\rho_1}) = m_1 \left[\frac{I_{PV}}{C_{pv1}} - \frac{y_2}{C_{pv1}} u_1 - \dot{y}_{1ref} \right] \qquad (30)$$

In this approach, $|S_1|^{\alpha_1}$ guarantees the convergence of the state trajectory to the sliding surface, and ρ_1 reduces the chattering effect by forcing the trajectory to stay on or close to the sliding surface. Finally, Equation (30) has been reorganized accordingly to extract the control input u_1 as shown:

$$u_1 = \frac{C_{pv1}}{m_1 y_2} \left[\frac{m_1 I_{PV}}{C_{pv1}} - m_1 \dot{y}_{1ref} + a_1 \, |S_1|^{\alpha_1} \, sign \, (\frac{S_1}{\rho_1}) \right] \qquad (31)$$

To design the BSMC for FC, a second sliding surface has been defined as:

$$S_2 = m_2\, e_2 \tag{32}$$

For the tracking of the fuel cell current y_4 to its desired value y_{4ref}, error term e_2 has been defined as follows:

$$e_2 = y_4 - y_{4ref} \tag{33}$$

Calculating the time derivative of Equation (32) results in the following expression:

$$\dot{S}_2 = m_2\, \dot{e}_2 \tag{34}$$

Taking time derivatives of error Equation (33) and substituting the value of $\dot{y}_4$ from Equation (11) gives:

$$\dot{e}_2 = -\frac{R_{FC}}{L_{FC}} y_4 + \frac{1}{L_{FC}} V_{FC} - \frac{1 - u_2}{L_{FC}} y_7 - \dot{y}_{4ref} \tag{35}$$

After substituting the value of $\dot{e}_2$ from Equation (35) in Equation (34), the following result has been generated:

$$\dot{S}_2 = m_2 \left[-\frac{R_{FC}}{L_{FC}} y_4 + \frac{1}{L_{FC}} V_{FC} - \frac{1 - u_2}{L_{FC}} y_7 - \dot{y}_{4ref} \right] \tag{36}$$

For the system to display asymptotic stability, the BSMC is derived in such a way that $\dot{S}_2$ is substituted and then equated with Equation (36) to obtain the following expression, where the adaptive barrier function gain a_2 for the sliding surface S_2 is defined by Equation (20):

$$\dot{S}_2 = -a_2\, |S_2|^{\alpha_2}\, sign\left(\frac{S_2}{\rho_2} \right) \tag{37}$$

$$-a_2\, |S_2|^{\alpha_2}\, sign\left(\frac{S_2}{\rho_2} \right) = m_2 \left[-\frac{R_{FC}}{L_{FC}} y_4 + \frac{1}{L_{FC}} V_{FC} - \frac{1 - u_2}{L_{FC}} y_7 - \dot{y}_{4ref} \right] \tag{38}$$

In Equation (38), $|S_2|^{\alpha_2}$ guarantees the convergence of the system to the designed sliding surface, whereas ρ_2 is employed to reduce the chattering effect. Finally, the last step is the control signal u_2 extraction from Equation (38), which can be written as:

$$u_2 = 1 + \frac{L_{FC}}{m_2 y_7} \left[-m_2 \frac{R_{FC}}{L_{FC}} y_4 + m_2 \frac{V_{FC}}{L_{FC}} - m_2 \dot{y}_{4ref} + a_2\, |S_2|^{\alpha_2}\, sign\left(\frac{S_2}{\rho_2} \right) \right] \tag{39}$$

For the derivation of the BSMC for the battery, a sliding surface has been modeled as:

$$S_3 = m_3\, e_3 \tag{40}$$

To track the battery current y_5 to its desired reference y_{5ref}, the error can be expressed as:

$$e_3 = y_5 - y_{5ref} \tag{41}$$

The time derivative of Equation (40) yields the following result:

$$\dot{S}_3 = m_3\, \dot{e}_3 \tag{42}$$

After taking the time derivative of error in Equation (41) and substituting the value of $\dot{y}_5$ from Equation (12), the final expression can be presented as:

$$\dot{e}_3 = \frac{-R_B}{L_B} y_5 + \frac{1}{L_B} V_{Bat} - \frac{u_{34}}{L_B} y_7 - \dot{y}_{5ref} \tag{43}$$

The substitution of $\dot{e}_3$ from Equation (43) in Equation (42) gives the following result:

$$\dot{S}_3 = m_3 \left[\frac{-R_B}{L_B} y_5 + \frac{1}{L_B} V_{Bat} - \frac{u_{34}}{L_B} y_7 - \dot{y}_{5ref} \right] \tag{44}$$

$\dot{S}_3$ has been replaced with the following expression for the asymptotic stability of the system, where the adaptive barrier function gain a_3 has been taken from Equation (20):

$$\dot{S}_3 = -a_3 \, |S_3|^{\alpha_3} \, sign\left(\frac{S_3}{\rho_3} \right) \tag{45}$$

$$-a_3 \, |S_3|^{\alpha_3} \, sign\left(\frac{S_3}{\rho_3} \right) = m_3 \left[\frac{-R_B}{L_B} y_5 + \frac{1}{L_B} V_{Bat} - \frac{u_{34}}{L_B} y_7 - \dot{y}_{5ref} \right] \tag{46}$$

Now, rearranging Equation (46) to find the control input u_{34} results in the following output:

$$u_{34} = \frac{L_B}{m_3 y_7} \left[-m_3 \frac{R_B}{L_B} y_5 + m_3 \frac{V_{Bat}}{L_B} - m_3 \dot{y}_{5ref} + a_3 \, |S_3|^{\alpha_3} \, sign\left(\frac{S_3}{\rho_3} \right) \right] \tag{47}$$

In this work, the SC has been employed to indirectly control the DC bus voltage V_{DC} since it provides high power transients in a short period [46]. To design the BSMC u_{56} for the SC, the sliding surface has been formulated as:

$$S_4 = m_4 \, e_4 + m_5 \, e_5 \tag{48}$$

where m_4 and m_5 are constants of the sliding surface with positive values, which are employed for controller design purposes. To track the SC current y_6 to its reference y_{6ref}, error terms are defined as follows:

$$e_4 = y_6 - y_{6ref} \tag{49}$$

$$e_5 = y_7 - y_{7ref} \tag{50}$$

The following expression shows the time derivative of Equation (23) required for determining the control law:

$$\dot{S}_4 = m_4 \, \dot{e}_4 + m_5 \, \dot{e}_5 \tag{51}$$

The time derivative of errors in Equations (49) and (50) has been investigated and substituted with the values of $\dot{y}_6$ and $\dot{y}_7$ from Equations (13) and (14) to result in the following expression:

$$\dot{e}_4 = \frac{-R_{SC}}{L_{SC}} y_6 + \frac{1}{L_{SC}} V_{SC} - \frac{u_{56}}{L_{SC}} y_7 - \dot{y}_{6ref} \tag{52}$$

$$\dot{e}_5 = \frac{1 - u_2}{C_o} y_4 + \frac{u_{34}}{C_o} y_5 + \frac{u_{56}}{C_o} y_6 - \frac{1}{C_o} i_o - \dot{y}_{7ref} \tag{53}$$

After substituting the values of $\dot{e}_4$ and $\dot{e}_5$ from Equations (52) and (53) in Equation (51), the derivative of the sliding surface can be expressed as:

$$\dot{S}_4 = m_4 \left[\frac{-R_{SC}}{L_{SC}} y_6 + \frac{1}{L_{SC}} V_{SC} - \frac{u_{56}}{L_{SC}} y_7 - \dot{y}_{6ref} \right] + m_5 \left[\frac{1 - u_2}{C_o} y_4 + \frac{u_{34}}{C_o} y_5 + \frac{u_{56}}{C_o} y_6 \right. $$
$$\left. - \frac{1}{C_o} i_o - \dot{y}_{7ref} \right] \tag{54}$$

$\dot{S}_4$ has been replaced with the following parameters and equated with Equation (54) to obtain the following expression, where the adaptive barrier function gain a_4 for the sliding surface S_4 has been taken from Equation (20):

$$\dot{S}_4 = -a_4 \, |S_4|^{\alpha_4} \, sign \left(\frac{S_4}{\rho_4} \right) \tag{55}$$

$$-a_4 \, |S_4|^{\alpha_4} \, sign \left(\frac{S_4}{\rho_4} \right) = m_4 \left[\frac{-R_{SC}}{L_{SC}} y_6 + \frac{1}{L_{SC}} V_{SC} - \frac{u_{56}}{L_{SC}} y_7 - \dot{y}_{6ref} \right] + m_5 \left[\frac{1 - u_2}{C_o} y_4 \right.$$
$$\left. + \frac{u_{34}}{C_o} y_5 + \frac{u_{56}}{C_o} y_6 - \frac{1}{C_o} i_o - \dot{y}_{7ref} \right] \tag{56}$$

To obtain the final expression for the control law u_{56}, Equation (56) has been organized as presented:

$$u_{56} = \frac{C_o L_{SC}}{C_o m_4 y_7 - L_{SC} m_5 y_6} \left[-m_4 \frac{R_{SC}}{L_{SC}} y_6 + m_4 \frac{V_{SC}}{L_{SC}} - m_4 \dot{y}_{6ref} + m_5 \frac{1 - u_2}{C_o} y_4 + m_5 \frac{u_{34}}{C_o} y_5 \right.$$
$$\left. - m_5 \frac{1}{C_o} i_o - m_5 \dot{y}_{7ref} + a_4 \, |S_4|^{\alpha_4} \, sign \left(\frac{S_4}{\rho_4} \right) \right] \tag{57}$$

Stability Analysis of the Nonlinear Controllers

The Lyapunov stability criteria for a system state that if the derivative of the positive definite Lyapunov candidate function considered for the stability analysis is negative semidefinite, the system exhibits asymptotic stability as the trajectory always approaches the origin with time [47]. To prove the stability of the system with the designed nonlinear controller, a positive definite Lyapunov candidate function has been formulated as:

$$V = \frac{1}{2} S_1^2 + \frac{1}{2} S_2^2 + \frac{1}{2} S_3^2 + \frac{1}{2} S_4^2 \tag{58}$$

Taking the time derivative of V from Equation (58) and substituting the values of $\dot{S}_1$, $\dot{S}_2$, $\dot{S}_3$ and $\dot{S}_4$ gives:

$$\dot{V} = S_1 \dot{S}_1 + S_2 \dot{S}_2 + S_3 \dot{S}_3 + S_4 \dot{S}_4 \tag{59}$$

Replacing the values of $\dot{S}_i$ in the above expression yields:

$$\dot{V} = S_1 [m_1 \, (\dot{y}_1 - \dot{y}_{1ref})] + S_2 [m_2 \, (\dot{y}_4 - \dot{y}_{4ref})] + S_3 [m_3 \, (\dot{y}_5 - \dot{y}_{5ref})] + S_4 [m_4 \, (\dot{y}_6 - \dot{y}_{6ref}) \\ + m_5 \, (\dot{y}_7 - \dot{y}_{7ref})] \tag{60}$$

Substituting the expressions for u_1, u_2, u_{34} and u_{56} in Equation (60) gives:

$$\dot{V} = -a_1 \, |S_1|^{\alpha_1} \underbrace{S_1 \, sign \left(\frac{S_1}{\rho_1} \right)}_{|S_1|} - \cdots - a_4 |S_4|^{\alpha_4} \underbrace{S_4 \, sign \left(\frac{S_4}{\rho_4} \right)}_{|S_4|} \tag{61}$$

$$\dot{V} = - \underbrace{a_1 \, |S_1|^{\alpha_1 + 1}}_{\geq 0} - \cdots - \underbrace{a_4 \, |S_4|^{\alpha_4 + 1}}_{\geq 0} \tag{62}$$

$$\dot{V} \leq 0 \tag{63}$$

In Equation (62), the controller gains and the absolute signum function are positive, which makes the time derivative of the Lyapunov function negative definite. This implies that the system always moves towards stability as the sliding surface approaches zero.

4. Results and Discussion

The aim of the nonlinear controllers implemented in this work is to generate a control signal which not only tracks the generated power from the DC–DC converters to the desired references but also expedites the regulation of the DC bus voltage. For comparison, the proposed BSMC and STSMCs have been simulated using MATLAB/Simulink® (2020b) with and without a disturbance to analyze their performance in more depth. Simulink allows

us to graphically evaluate the designed system before testing it on real-time applications; therefore, this platform has been used to verify the effectiveness of the system presented. The controllers U_i extracted in Section 3 represent the control signals used to generate the duty cycle accordingly through the PWM generator in Simulink to be provided to the inputs of the switches of the respective converters. The frequency of the signals used in this work is 10 kHz in Simulink. The ODE45 solver has been used with a variable step size to evaluate the controller's performance using the control signals u_1, u_2, u_{34} and u_{56} mathematically designed and extracted in the previous section. These control signals act as a switch for the DC–DC converters designed in Simulink. For the Simulink implementation of these controllers and DC–DC converters, their gains and parameters are given in Table 2. For this system, the law of conservation of power can be expressed as:

$$P_{Grid} = P_D - (P_{FC} + P_{Bat} + P_{SC}) \tag{64}$$

$$P_D = P_{Load} - P_{PV} \tag{65}$$

In Equation (64), P_{Grid} is the power that is taken from the grid or provided to the grid. P_{FC}, P_{Bat} and P_{SC} are the power provided by the FC, battery and SC, respectively. As given in Equation (65), power demand P_D can display two cases: it can be negative when P_{PV} is sufficient to meet the load requirements, and the additional power can be either provided to the grid or consumed to charge the battery/SC. On the other hand, P_D can be positive, which means that the additional power to fulfil the load demand is supplied by the HESS, FC and grid. The FC, battery and SC combine to fulfil the power demand in the following pattern:

- The SC is responsible for the regulation of the DC bus voltage since it is the fastest power source and provides instant power during high power transients.
- The battery is responsible for keeping the SC charged since it is known for its high energy density. Simultaneously, it also discharges to contribute towards the power demand.
- The FC is the primary energy source that charges the battery and provides power to the grid in case the battery and SC are nominally charged during low power demand.

Table 2. Specifications of the designed system.

DC–DC Converter Parameters	
L_{pv}, L_{FC}, L_B, L_{SC}	3.3 mH, 3.3 mH, 3.3 mH, 3.3 mH
R_{FC}, R_B, R_{SC}	20 mΩ, 20 mΩ, 20 mΩ
C_{pv1}, C_{pv2}, C_o	68 µF, 68 µF, 68 µF
Switching frequency	10 kHz
BSMC parameters	
m_1, m_2, m_3, m_4, m_5	0.05, 0.05, 0.03, 0.05, 0.01
$\bar{a}_1$, $\bar{a}_2$, $\bar{a}_3$, $\bar{a}_4$	1000, 1000, 100, 1000
ε	0.002

The power provided by the PV system is presented in Figure 4 under varying irradiance and temperature conditions operating at its maximum power point (MPP). Since this is the only stochastic energy source in this system, the additional power is now supplied by the remaining energy generation and storage sources. Figure 5 illustrates the power provided by the SC along with the role of the BSMC and SMC in tracking the reference power. Initially, at $t = 0$ s, the SC is charged during comparatively low power demand, after which its active performance can be observed as it discharges during high power transients or remains idle accordingly. At the same time, one can also observe the efficient working of the BSMC in tracking SC power to its reference over the STSMC, which displays several overshoots and undershoots.
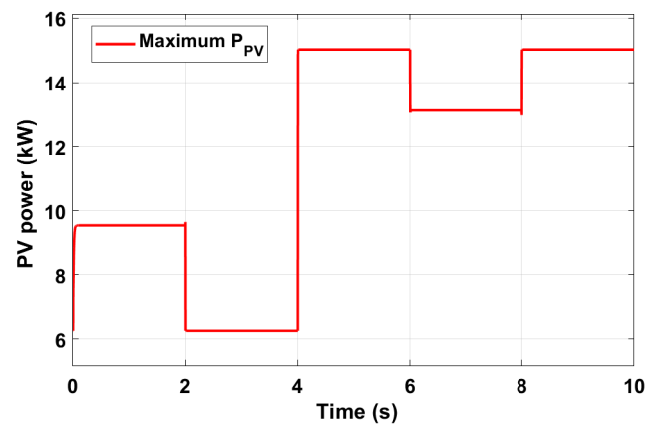
**Figure 4.** Generated power from the PV source operating at MPP.
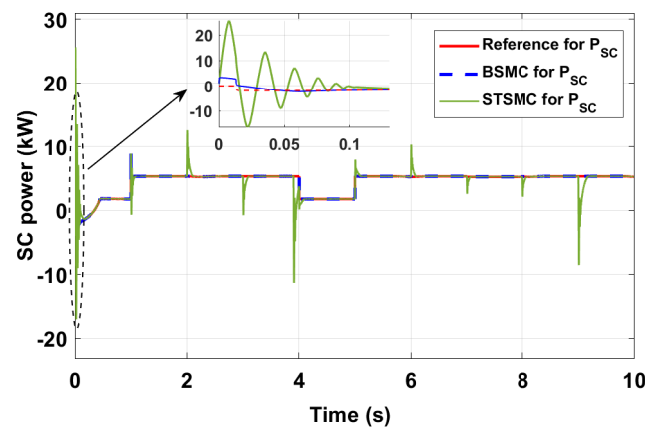
Figure 5. SC response to the additional power demand: BSMC and STSMC performance.

One of the objectives of this work focused on the reduction in chattering exhibited by most of the sliding mode controllers. To verify it, the phenomenon of chattering displayed in the SC's response with the BSMC and STSMC is presented in Figure 6. As the SC is responsible for providing power during high power transients, it is affected the most during external disturbance, which can be observed in the form of sinusoidal movement of the state trajectory. It can be observed that while the STSMC displays noticeable chattering in its tracking, the BSMC effectively minimizes the chattering close to almost negligible in this case.
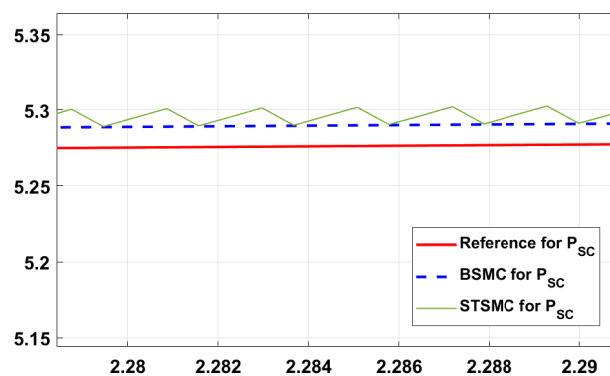
Figure 6. Zoomed-in view of chattering displayed in SC's response with BSMC and STSMC.

The power provided by the battery to charge the SC under varying power demand conditions is displayed in Figure 7. Under high power demand, the battery supports SC by discharging depending on its state of charge (SoC). In this case, both the BSMC and STSMCs exhibit similar performance but with a delayed steady-state response by the STSMC. Figure 8 shows the overall contribution of FC power. Since it is the main source responsible for keeping the battery and SC charged, the FC always provides variable power to maintain the power balance, during which the BSMC plays an important role. The main objective of designing a power management system and controllers is to regulate the DC link voltage portrayed in Figure 9. The V$_{DC}$ reference is set to 400 V, and the tracking of both controllers is illustrated in the graph. It is worth noticing their transient responses in which the STSMC exhibits a peak voltage of 421 V, whereas the BSMC shows a negligible peak.
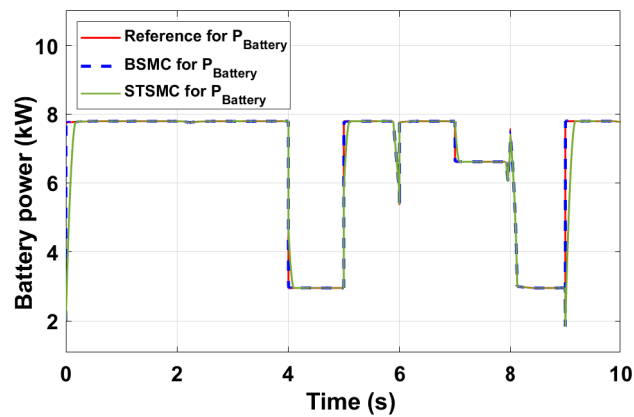
Figure 7. Battery response to the additional power demand: BSMC and STSMC performance.
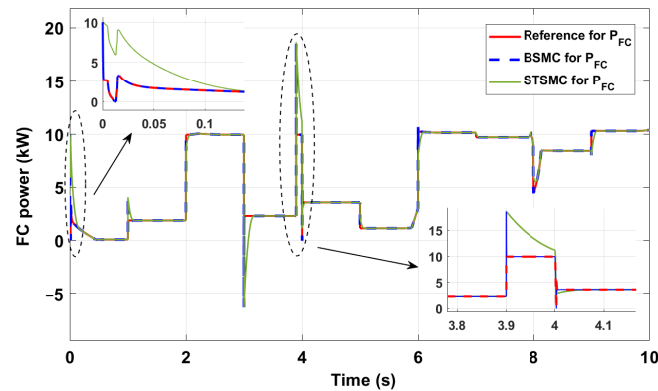
Figure 8. FC response to the additional power demand: BSMC and STSMC performance.

In the upcoming results, the performance exhibited by both controllers is displayed in the presence of a sinusoidal disturbance with a varying amplitude shown in Figure 10. This induced disturbance in the study represents a disturbance with an unknown upper bound, which might affect the states due to some parametric variations in the inductor, capacitor or resistor values over time, or it can be a disturbance due to some external environmental factors. It can be mathematically modeled as:

$$\eta(t) = \begin{cases} 450\,sin(t), & if \ \ t \leqslant 3\,s \\ 510\,sin(t), & if \ \ 3\,s < t \leqslant 6\,s \\ 570\,sin(t), & if \ \ t > 6\,s \end{cases} \tag{66}$$
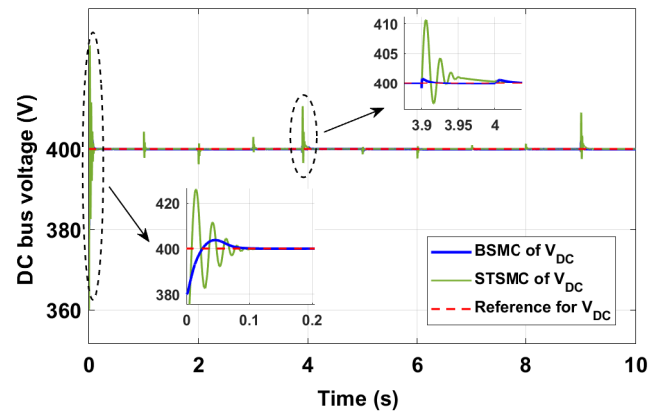
**Figure 9.** Regulation of DC bus voltage: BSMC and STSMC performance.
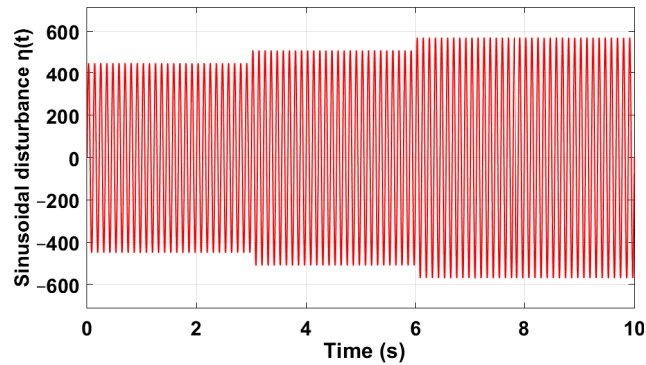
Figure 10. Sinusoidal disturbance with increasing amplitude $\eta(t)$.

Figures 11 and 12 present the tracking of the SC and battery power to their references with both controllers in the presence of the disturbance introduced in the system to test their robustness. Since the SC is responsible for providing power during high transients, the tracking of the STSMC is affected the most in the presence of disturbance as displayed in both figures. However, the output power tracked by the controllers exhibits a sinusoidal movement around the provided power references, which is due to the sinusoidal nature of the disturbance and does not exceed the peak-to-peak voltage of 1 V.
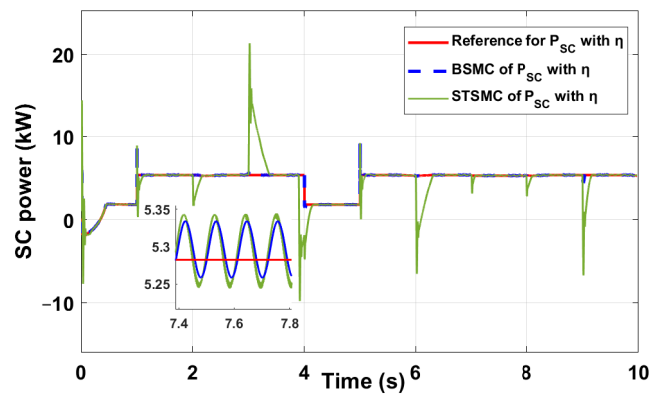
Figure 11. SC response to the additional power demand: BSMC and STSMC performance in the presence of disturbance $\eta(t)$.
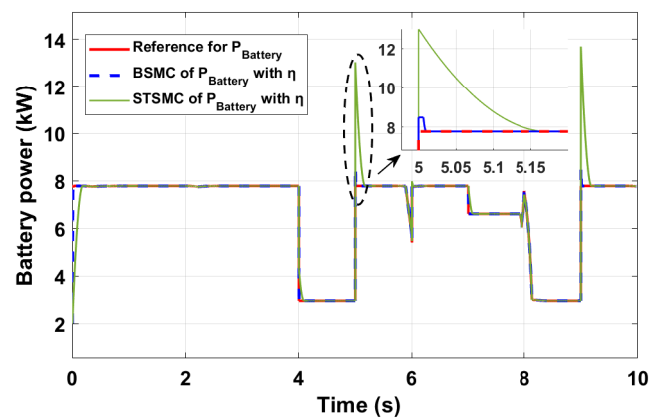
Figure 12. Battery response to the additional power demand: BSMC and STSMC performance in the presence of disturbance $\eta(t)$.

Figures 13 and 14 illustrate the tracking of FC power and DC bus voltage regulation, respectively. STSMC displays major overshoots and undershoots in both cases due to the nonlinear term present in the reaching law of the STSMC [44]. The zoomed-in views of the graph verify the superior performance of the BSMC over the STSMC in which the variations displayed by the latter controller range between 20 V to -20 V during the regulation of the DC bus voltage. A graph illustrating the individual contributions of each source in different scenarios to fulfil the power demand is presented in Figure 15. The sources charge and discharge themselves corresponding to the power demand while drawing or injecting power into the grid according to the power availability. It is worth noticing that in all the cases, the power balance is always maintained, i.e., the sum of power at any time instant is equal to the power demand, which helps achieve the goal of the designed framework.
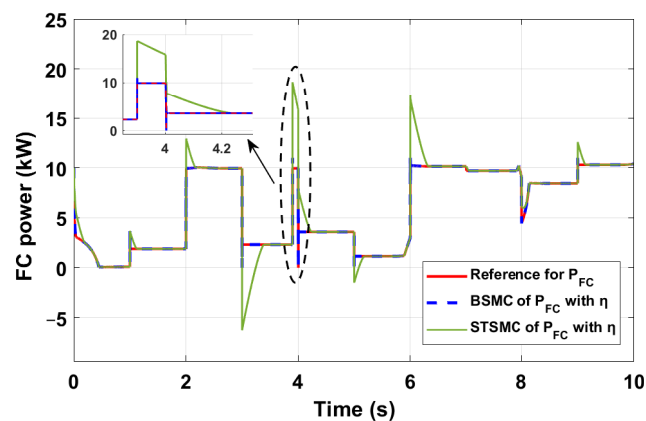

Figure 13. FC response to the additional power demand: BSMC and STSMC performance in the presence of disturbance $\eta(t)$.
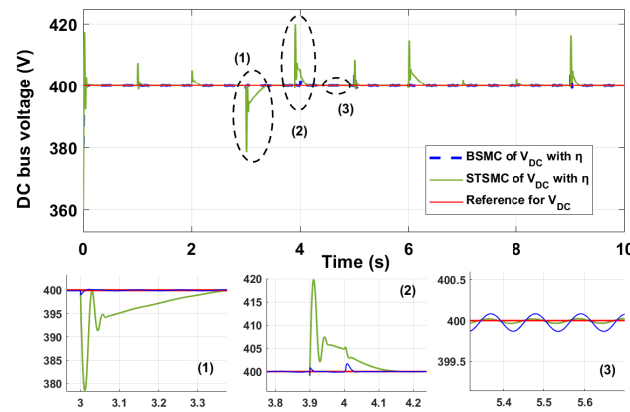
Figure 14. Regulation of DC bus voltage: BSMC and STSMC performance in the presence of disturbance $\eta(t)$.
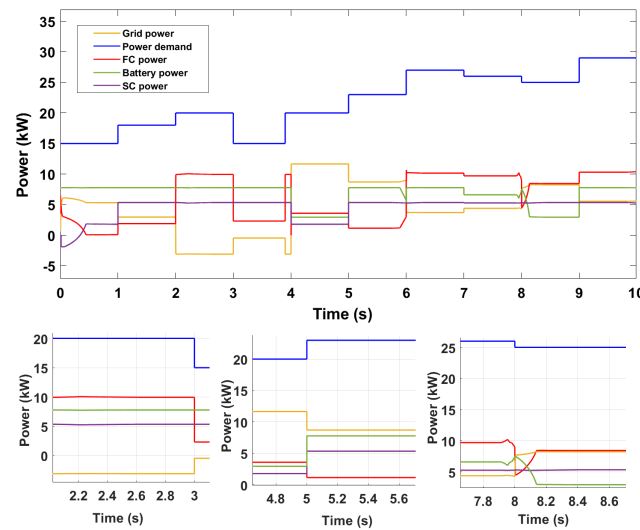

Figure 15. Grid power with varying load demand and generated power.

5. BSMC Validation with Experimental Data

The sliding mode control has proven its high efficiency, and it indeed provides closed-loop insensitivity to the disturbances and guarantees finite-time convergence [43]. However, the implementation of the first order sliding mode controllers (FOSMCs) requires knowledge of the upper bound of disturbances. In practice, this bound is not constant and, moreover, frequently it is unknown. This means that the gains of the FOSMCs are overestimated. This is a main obstacle in FOSMC implementation leading to a growth in the undesired chattering effect. For this reason, the BSMC has been employed in recent research works, as it avoids the overestimation of the gains by adapting them according to the trajectory of the sliding surface. To ensure a fair comparison of the controllers under similar conditions, the gains employed for the BSMC, STSMC [44] and SMC [30] have been set as the same under various conditions. To further verify the robustness of the BSMC, experimental data of real PV profile data have been taken from the MultiGood MicroGridLAB (MG2lab) in Politecnico di Milano, Italy, and the performance of a basic SMC has been compared with each STSMC and BSMC designed in the previous section. To run the entire PV profile exhibiting the variations throughout the day under varying solar irradiance and temperature conditions, a complete 24 h profile has been reshaped for 24 s to implement it smoothly in the MATLAB/Simulink environment with a nonlinear controller with an ODE23 solver as shown in Figure 16. The generated control signal u_1 from the BSMC is used to generate maximum power from the PV source, and, since this

renewable energy source is only generating power, the chattering displayed by this control signal u_1 is very minute as shown in Figure 17.
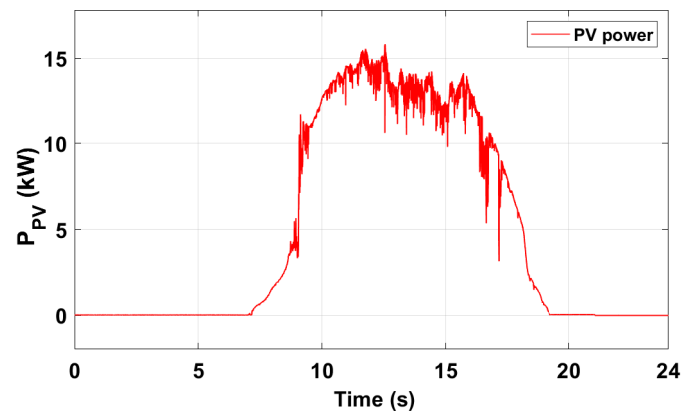

**Figure 16.** Experimental PV power profile.
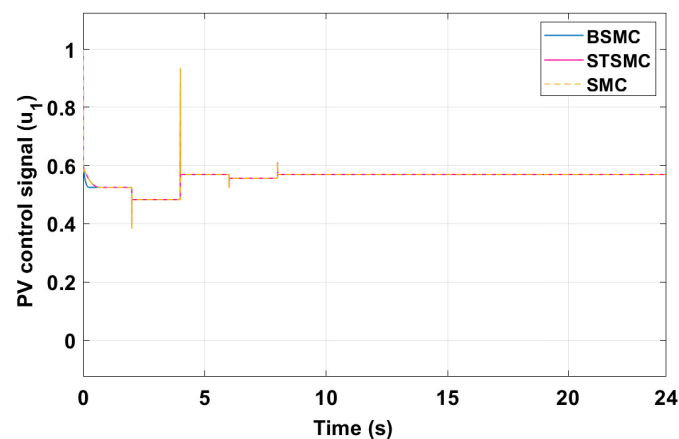
Figure 17. PV control signal u_1.

Figures 18 and 19 illustrate the tracking performance of the SMC, STSMC and BSMC for SC to assess their robustness with experimental data displaying multiple variations and their corresponding control signals u_{56}, respectively. Initially, during low load demand, the SC charges or stays idle, during which the BSMC tracks the reference power perfectly. At the same time, the SMC and STSMC exhibit a notably large transient voltage. Since the SC is responsible for power during high transient states, there are multiple fluctuations displayed by the SMC and STSMC between $t = 10$ s to $t = 15$ s as shown in the zoomed-in graphs of Figure 18 due to variations in the PV power, while the BSMC displays negligible fluctuations in its tracking. Despite this effect, the controllers track the output power to the provided power references. It is worth noting that the performance of the BSMC remains exceptional under all conditions, with a maximum overshoot voltage of 4 V, while the SMC and STSMC display overshoot voltages between 23 V and 16 V, respectively.
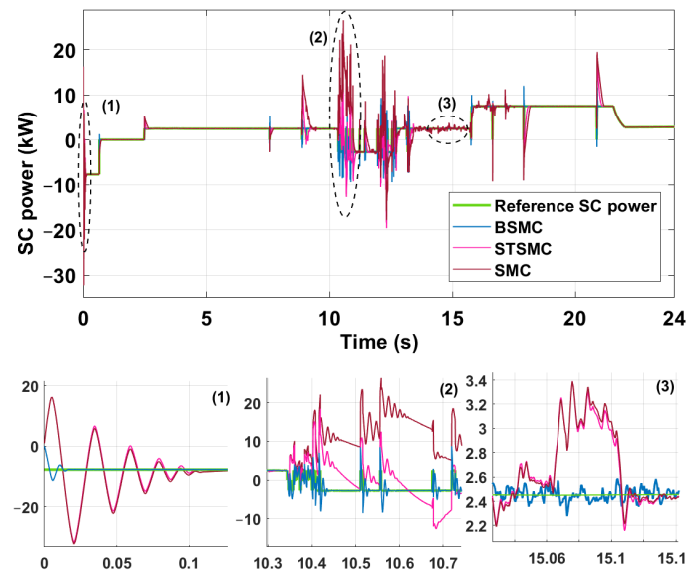
**Figure 18.** SC power: BSMC vs. STSMC vs. SMC performance with experimental data.
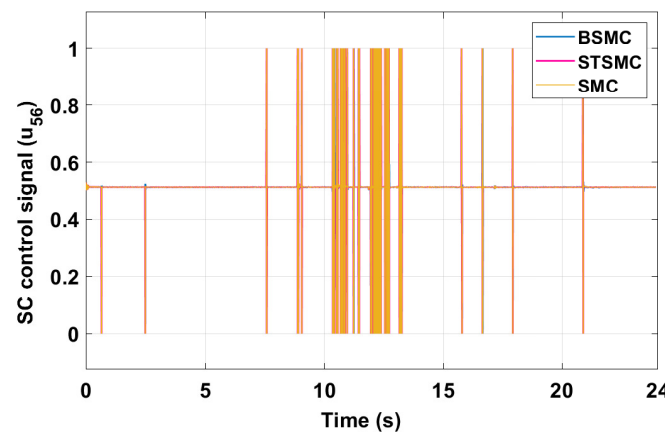
Figure 19. SC control signal u_{56}.

In Figures 20 and 21, the tracking performance of the SMC, STSMC and BSMC for the battery power to its reference is presented to evaluate their robustness with experimental data along with their corresponding control signals u_{34}. At t = 0 s, the BSMC starts tracking its reference battery power, while the SMC and STSMC lag the tracking for a few seconds. During high power fluctuation time between t = 10 s to t = 15 s, large overshoots and undershoots by the SMC and STSMC are displayed, ranging from 30 V to 12 V, while the BSMC exhibits effective performance by limiting the overshoot limit within 5 V, and the corresponding chattering in the control signals can be noticed in Figure 21. In the zoomed-in graphs for the battery power tracking, the smooth tracking of the BSMC compared to other controllers can be clearly observed as the battery exhibits multiple power variations to fulfil the load demand under varying PV power supply conditions. However, all the controllers track the output power to the provided power references despite the power fluctuations.

In Figures 22 and 23, the performance exhibited by the SMC, STSMC and BSMC for the FC power tracking to its corresponding reference is illustrated to verify their robustness with experimental data along with their control signals u_2. Since the FC is responsible for compensating the power differences between the demand and the power provided by the hybrid energy storage system, multiple fluctuations can be observed in the graph. At t = 8.8 s, the tracking of FC power to its reference exhibited by the BSMC can be observed in the zoomed-in graph. At the same time, the SMC and STSMC lag the tracking by differences

of approximately 20 V and 18 V, respectively. During high power fluctuation time between $t = 10$ s to $t = 15$ s, large overshoots and undershoots by the SMC and STSMC are displayed, ranging from 40 V to 35 V, while the BSMC exhibits effective performance by limiting the overshoot limit to within 3 V of the corresponding chattering in the control signals shown in Figure 23. In the zoomed-in graphs for the FC power tracking, the smooth tracking of the BSMC compared to other controllers can be clearly observed as the FC exhibits multiple power variations to fulfil the load demand under varying hybrid energy storage supply conditions.
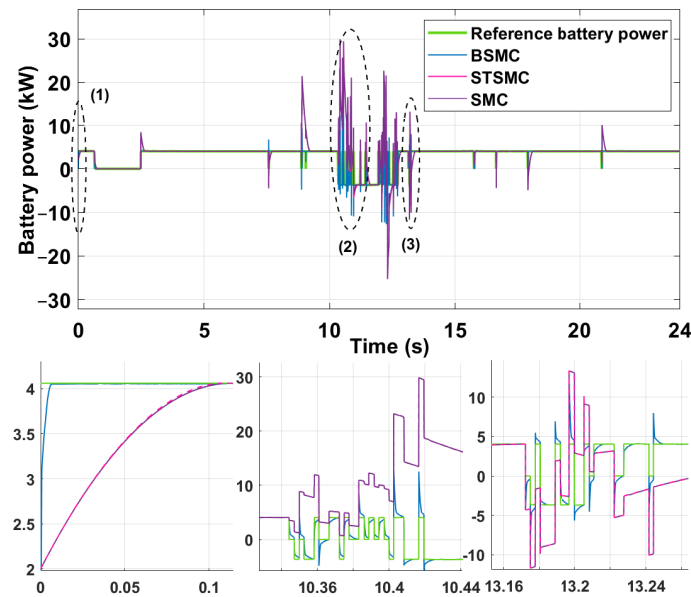

**Figure 20.** Battery power: BSMC vs. STSMC vs. SMC performance with experimental data.
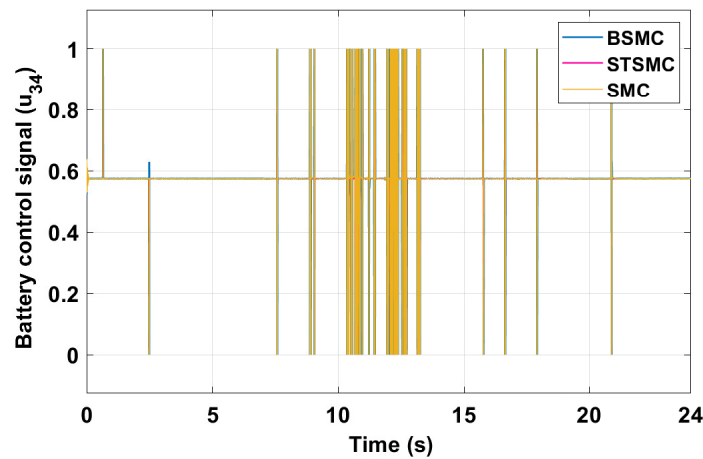
Figure 21. Battery control signal u_{34}.

Lastly, the regulation of DC bus voltage V_{DC} at 400 V by the SMC, STSMC and BSMC is illustrated by Figure 24. SMS and STSMC display visibly large steady-state errors at $t = 0$ s, whereas the BSMC shows negligible deviations from its tracking. During power fluctuations between $t = 10$ s to $t = 15$ s as seen in the previous results, the BSMC displays fluctuations within 4 V, whereas the SMC and STSMC deviate by exhibiting undershoots of 9 V and 5 V, respectively. For the entire period of $t = 0$ s to $t = 24$ s, the performance exhibited by the BSMC is worth noticing as it regulates the DC bus voltage near its reference voltage of 400 V. Moreover, a numerical analysis of the SMC, STSMC and BSMC is presented in Table 3. It is worth noticing that the BSMC displays small deviations in peak voltages,

overshoots, steady-state error and settling time. In contrast, the SMC and STSMC exhibit comparatively large variations, i.e., 28.89% and 24.6% steady-state errors, respectively.
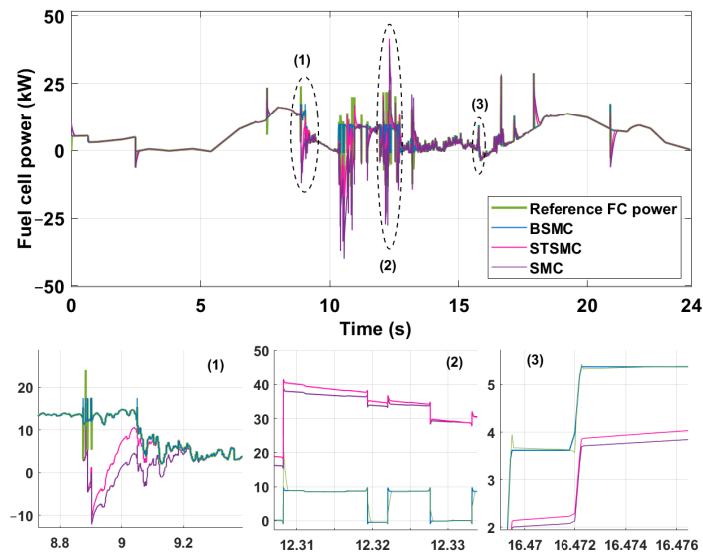

Figure 22. Fuel cell power: BSMC vs. STSMC vs. SMC performance with experimental data.
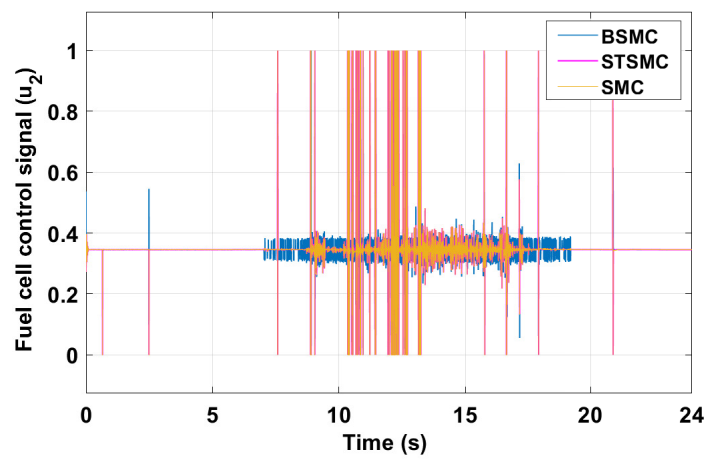

Figure 23. Fuel cell control signal u_2.

Table 3. Quantitative analysis of SMC, STSMC and BSMC for DC bus voltage regulation.

| Controllers	Settling Time (s)	Overshoot (%)	Steady-State Error (%)	Peak Voltage (V)
SMC	0.1	22.18	28.98	411.36
STSMC	0.09	21.48	24.6	408.61
BSMC	0.03	13.56	4	402.03
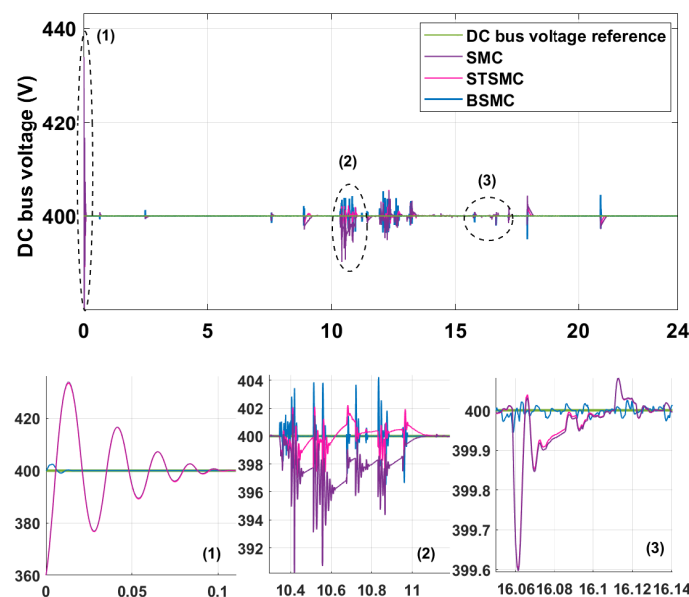
Figure 24. DC bus voltage: BSMC vs. STSMC vs. SMC performance with experimental data.

6. Conclusions

This study integrated and controlled photovoltaics (PV), a fuel cell (FC), a battery and a supercapacitor (SC) to meet a conventional load demand within a grid-connected microgrid. The proposed approach implements a robust barrier sliding mode controller (BSMC) as a primary-level control to regulate power according to references set by an AI-based energy management unit. The achievements of this work have been presented through results, which demonstrate that the SC effectively regulates the DC bus voltage at 400 V, while the battery both charges the SC and supplies power to fulfil overall demand. The FC enhances the hybrid storage system and maintains battery charge during high power demand. Moreover, the BSMC exhibits impressive performance in the presence of sinusoidal disturbances with varying amplitudes.

For comparison, further simulations were conducted to compare the BSMC with a sliding mode controller (SMC) and an advanced variant, the supertwisting sliding mode controller (STSMC), using MATLAB/Simulink® (2020b). These comparisons were carried out across various power demand step changes using a real experimental PV profile with varying solar irradiance and temperature. Results revealed that the SMC and STSMC exhibited fluctuations and displayed various undershoots/overshoots during power tracking. In contrast, the BSMC demonstrated stable regulation of the DC bus voltage, showcasing its suitability for complex systems susceptible to disturbances and uncertainties. The findings of this work show that the BSMC effectively maintained stable DC bus voltage regulation under diverse conditions within grid-connected systems, even in the presence of significant external disturbances, leading to substantial fluctuations in the DC bus voltage. To conclude, the system overall ensured coordinated power generation by PV, the FC and the energy storage system to meet power demands, which also makes it suitable for integration within the primary control level of a system-of-systems (SoS) framework for microgrids. Future work includes applying this technique to systems integrating hydrogen-based energy generation units alongside multi-input multi-output DC–DC converters, thereby enabling autonomous operations.

Author Contributions: Conceptualization, S.S.Z. and M.M.; methodology, S.S.Z.; software, S.S.Z., A.D. and M.A.A.; validation, S.S.Z. and M.M.; formal analysis, S.S.Z. and A.D.; investigation, A.D. and M.A.A.; resources, S.S.Z. and M.M.; data curation, M.M.; writing—original draft preparation, S.S.Z.; writing—review and editing, M.A.A. and M.M.; visualization, S.S.Z.; supervision, M.M.; funding acquisition, M.M. All authors have read and agreed to the published version of the manuscript.

Data Availability Statement: Data will be provided on request.

Conflicts of Interest: The authors declare no conflict of interest.

Abbreviations

EMS	Energy management system
DC	Direct current
PV	Photovoltaics
HESS	Hybrid energy storage system
RESs	Renewable energy sources
MPPT	Maximum power point tracking
SC	Supercapacitor
FC	Fuel cell
SoC	State of charge
SMC	Sliding mode controller
STSMC	Super-twisting sliding mode controller
BSMC	Barrier function-dependent sliding mode controller
V_{PV_i}	Input PV voltage to converter
V_{PV_o}	Output PV voltage from converter
I_{PV}	PV panel current
V_{FC}, I_{FC}	Voltage and current of the fuel cell
V_{Bat}, I_{Bat}	Voltage and current of the battery
V_{SC}, I_{SC}	Voltage and current of the supercapacitor
V_{DC}	Voltage of the DC bus
P_D	Power demand
$\eta(t)$	Sinusoidal disturbance
$\dot{y}_{i=1,..,7}$	State-space model for V_{PV_i}, I_{PV}, V_{PV_o}, I_{FC}, I_{Bat}, I_{SC} and V_{DC}, respectively
Sign	Signum function
C_{pv1}, C_{pv2}	Input and output capacitance of PV converter
C_o	Output capacitance
L_{PV}	Inductance of PV converter
L_{FC}, L_B, L_{SC}	Inductance of FC, battery and SC converters
R_{FC}, R_B, R_{SC}	Resistance of FC, battery and SC converters
$S_{i=1,...,6}$	Converter switches
S_i	Sliding surfaces
$m_{i=1,...,5}$	Design constants of sliding surfaces
y_{iref}	Reference currents provided by EMS
e_i	Error between state and reference currents
$a_{i=1,...,4}$	Adaptive controller gains
$\alpha_{i=1,...,4}$, $\rho_{i=1,...,4}$	Sliding surface-reaching law constant
ε	Constant in close vicinity of zero
$u_{1,2,34,56}$	Control signals

References

1. Khezri, M.; Heshmati, A.; Khodaei, M. Environmental implications of economic complexity and its role in determining how renewable energies affect CO_2 emissions. *Appl. Energy* **2022**, *306*, 117948. [CrossRef]
2. Zhong, J.; Bollen, M.; Rönnberg, S. Towards a 100% renewable energy electricity generation system in Sweden. *Renew. Energy* **2021**, *171*, 812–824. [CrossRef]
3. Aqachmar, Z.; Sassi, H.B.; Lahrech, K.; Barhdadi, A. Solar technologies for electricity production: An updated review. *Int. J. Hydrogen Energy* **2021**, *46*, 30790–30817. [CrossRef]
4. Nespoli, A.; Leva, S.; Mussetta, M.; Ogliari, E.G.C. A Selective Ensemble Approach for Accuracy Improvement and Computational Load Reduction in ANN-Based PV Power Forecasting. *IEEE Access* **2022**, *10*, 32900–32911. [CrossRef]
5. Elmorshedy, M.F.; Elkadeem, M.; Kotb, K.M.; Taha, I.B.; Mazzeo, D. Optimal design and energy management of an isolated fully renewable energy system integrating batteries and supercapacitors. *Energy Convers. Manag.* **2021**, *245*, 114584. [CrossRef]

6.   Rezaei, H.; Abdollahi, S.E.; Abdollahi, S.; Filizadeh, S. Energy managment strategies of battery-ultracapacitor hybrid storage systems for electric vehicles: Review, challenges, and future trends. *J. Energy Storage* **2022**, *53*, 105045. [CrossRef]

7.   Lei, M.; Mohammadi, M. Hybrid machine learning based energy policy and management in the renewable-based microgrids considering hybrid electric vehicle charging demand. *Int. J. Electr. Power Energy Syst.* **2021**, *128*, 106702. [CrossRef]

8.   Fu, Z.; Zhu, L.; Tao, F.; Si, P.; Sun, L. Optimization based energy management strategy for fuel cell/battery/ultracapacitor hybrid vehicle considering fuel economy and fuel cell lifespan. *Int. J. Hydrogen Energy* **2020**, *45*, 8875–8886. [CrossRef]

9.   Veeramsetty, V.; Chandra, D.R.; Grimaccia, F.; Mussetta, M. Short Term Electric Power Load Forecasting Using Principal Component Analysis and Recurrent Neural Networks. *Forecasting* **2022**, *4*, 149–164. [CrossRef]

10.   Mansoor, M.; Grimaccia, F.; Leva, S.; Mussetta, M. Comparison of echo state network and feed-forward neural networks in electrical load forecasting for demand response programs. *Math. Comput. Simul.* **2021**, *184*, 282–293. [CrossRef]

11.   Yang, Y.; Bremner, S.; Menictas, C.; Kay, M. Modelling and optimal energy management for battery energy storage systems in renewable energy systems: A review. *Renew. Sustain. Energy Rev.* **2022**, *167*, 112671. [CrossRef]

12.   Dubal, D.P.; Ayyad, O.; Ruiz, V.; Gomez-Romero, P. Hybrid energy storage: The merging of battery and supercapacitor chemistries. *Chem. Soc. Rev.* **2015**, *44*, 1777–1790. [CrossRef] [PubMed]

13.   Wang, J.; Wang, B.; Zhang, L.; Wang, J.; Shchurov, N.; Malozyomov, B. Review of bidirectional DC–DC converter topologies for hybrid energy storage system of new energy vehicles. *Green Energy Intell. Transp.* **2022**, *1*, 100010. [CrossRef]

14.   Kondrath, N. An overview of bidirectional DC-DC converter topologies and control strategies for interfacing energy storage systems in microgrids. *J. Electr. Eng.* **2018**, *6*, 11–17. [CrossRef]

15.   İnci, M.; Savrun, M.M.; Çelik, Ö. Integrating electric vehicles as virtual power plants: A comprehensive review on vehicle-to-grid (V2G) concepts, interface topologies, marketing and future prospects. *J. Energy Storage* **2022**, *55*, 105579. [CrossRef]

16.   Keskin, R.; Aliskan, I.; Daş, E. Robust structured controller synthesis for interleaved boost converters using an h∞ control method. *Trans. Inst. Meas. Control* **2021**, *43*, 3169–3180. [CrossRef]

17.   Rajabi, A.; Shahir, F.M.; Sedaghati, R. New unidirectional step-up DC-DC converter for fuel-cell vehicle: Design and implementation. *Electr. Power Syst. Res.* **2022**, *212*, 108653. [CrossRef]

18.   Mahmoud, M.S.; Saif Ur Rahman, M.; AL-Sunni, F.M. Review of microgrid architectures—A system of systems perspective. *IET Renew. Power Gener.* **2015**, *9*, 1064–1078. [CrossRef]

19.   Shi, R.; Li, S.; Zhang, P.; Lee, K.Y. Integration of renewable energy sources and electric vehicles in V2G network with adjustable robust optimization. *Renew. Energy* **2020**, *153*, 1067–1080. [CrossRef]

20.   Zehra, S.S.; Rahman, A.U.; Grimaccia, F.; Niccolai, A.; Mussetta, M. Neuro-fuzzy based energy management of PV-FC based grid-connected microgrid for e-mobility. In Proceedings of the 2022 IEEE International Conference on Environment and Electrical Engineering and 2022 IEEE Industrial and Commercial Power Systems Europe (EEEIC/I&CPS Europe), Prague, Czech Republic, 28 June–1 July 2022; pp. 1–6. [CrossRef]

21.   Patel, S.; Ghosh, A.; Ray, P.K. Improved power flow management with proposed fuzzy integrated hybrid optimized fractional order cascaded proportional derivative filter (1+ proportional integral) controller in hybrid microgrid systems. *ISA Trans.* **2023**, *136*, 742–754. [CrossRef]

22.   Malik, S.M.; Sun, Y.; Hu, J. An adaptive virtual capacitive droop for hybrid energy storage system in DC microgrid. *J. Energy Storage* **2023**, *70*, 107809. [CrossRef]

23.   Wu, Y.; Isidori, A.; Lu, R.; Khalil, H.K. Performance recovery of dynamic feedback-linearization methods for multivariable nonlinear systems. *IEEE Trans. Autom. Control* **2019**, *65*, 1365–1380. [CrossRef]

24.   Lam, Q.L.; Bratcu, A.I.; Riu, D.; Boudinet, C.; Labonne, A.; Thomas, M. Primary frequency H∞ control in stand-alone microgrids with storage units: A robustness analysis confirmed by real-time experiments. *Int. J. Electr. Power Energy Syst.* **2020**, *115*, 105507. [CrossRef]

25.   Adil, H.M.M.; Ahmed, S.; Ahmad, I. Control of MagLev system using supertwisting and integral backstepping sliding mode algorithm. *IEEE Access* **2020**, *8*, 51352–51362. [CrossRef]

26.   Iovine, A.; Carrizosa, M.J.; Damm, G.; Alou, P. Nonlinear control for DC microgrids enabling efficient renewable power integration and ancillary services for AC grids. *IEEE Trans. Power Syst.* **2018**, *34*, 5136–5146. [CrossRef]

27.   Holari, Y.T.; Taher, S.A.; Mehrasa, M. Power management using robust control strategy in hybrid microgrid for both grid-connected and islanding modes. *J. Energy Storage* **2021**, *39*, 102600. [CrossRef]

28.   Badar, M.; Ahmad, I.; Mir, A.A.; Ahmed, S.; Waqas, A. An autonomous hybrid DC microgrid with ANN-fuzzy and adaptive terminal sliding mode multi-level control structure. *Control Eng. Pract.* **2022**, *121*, 105036. [CrossRef]

29.   Rahman, A.U.; Zehra, S.S.; Ahmad, I.; Armghan, H. Fuzzy supertwisting sliding mode-based energy management and control of hybrid energy storage system in electric vehicle considering fuel economy. *J. Energy Storage* **2021**, *37*, 102468. [CrossRef]

30.   Abianeh, A.J.; Ferdowsi, F. Sliding mode control enabled hybrid energy storage system for islanded dc microgrids with pulsing loads. *Sustain. Cities Soc.* **2021**, *73*, 103117. [CrossRef]

31.   Mousavi, Y.; Bevan, G.; Kucukdemiral, I.B.; Fekih, A. Sliding mode control of wind energy conversion systems: Trends and applications. *Renew. Sustain. Energy Rev.* **2022**, *167*, 112734. [CrossRef]

32.   Cavallo, A.; Canciello, G.; Guida, B.; Kulsangcharoen, P.; Yeoh, S.S.; Rashed, M.; Bozhko, S. Multi-objective supervisory control for dc/dc converters in advanced aeronautic applications. *Energies* **2018**, *11*, 3216. [CrossRef]

33. Cavallo, A.; Canciello, G.; Russo, A. Integrated supervised adaptive control for the more Electric Aircraft. *Automatica* **2020**, *117*, 108956. [CrossRef]

34. Ali, N.; Liu, Z.; Armghan, H.; Armghan, A. Double integral sliding mode controller for wirelessly charging of fuel cell-battery-super capacitor based hybrid electric vehicle. *J. Energy Storage* **2022**, *51*, 104288. [CrossRef]

35. Oliveira, T.R.; Hsu, L.; Nunes, E.V.L. Smooth sliding control to overcome chattering arising in classical SMC and super-twisting algorithm in the presence of unmodeled dynamics. *J. Frankl. Inst.* **2022**, *359*, 1235–1256. [CrossRef]

36. Ahmed, I.; Adil, H.M.M.; Ahmed, S.; Ahmad, I.; Rehman, Z. Robust nonlinear control of battery electric vehicle charger in grid to vehicle and vehicle to grid applications. *J. Energy Storage* **2022**, *52*, 104813. [CrossRef]

37. Shtessel, Y.; Edwards, C.; Fridman, L.; Levant, A. *Sliding Mode Control and Observation*; Springer: Berlin/Heidelberg, Germany, 2014; Volume 10.

38. Lu, J.; Savaghebi, M.; Ghias, A.M.; Hou, X.; Guerrero, J.M. A reduced-order generalized proportional integral observer-based resonant super-twisting sliding mode control for grid-connected power converters. *IEEE Trans. Ind. Electron.* **2020**, *68*, 5897–5908. [CrossRef]

39. Obeid, H.; Fridman, L.M.; Laghrouche, S.; Harmouche, M. Barrier function-based adaptive sliding mode control. *Automatica* **2018**, *93*, 540–544. [CrossRef]

40. Zehra, S.S.; Wood, M.J.; Grimaccia, F.; Mussetta, M. A Cost-Effective Fuzzy-based Demand-Response Energy Management for Batteries and Photovoltaics. In Proceedings of the 2023 11th International Conference on Smart Grid (icSmartGrid), Paris, France, 4–7 June 2023; IEEE: Piscataway, NJ, USA, 2023; pp. 1–6.

41. Zehra, S.S.; Rahman, A.U.; Armghan, H.; Ahmad, I.; Ammara, U. Artificial intelligence-based nonlinear control of renewable energies and storage system in a DC microgrid. *ISA Trans.* **2022**, *121*, 217–231. [CrossRef] [PubMed]

42. Arsalan, M.; Iftikhar, R.; Ahmad, I.; Hasan, A.; Sabahat, K.; Javeria, A. MPPT for photovoltaic system using nonlinear backstepping controller with integral action. *Sol. Energy* **2018**, *170*, 192–200. [CrossRef]

43. Drakunov, S.V.; Utkin, V.I. Sliding mode control in dynamic systems. *Int. J. Control* **1992**, *55*, 1029–1037. [CrossRef]

44. Sami, I.; Ullah, S.; Amin, S.U.; Al-Durra, A.; Ullah, N.; Ro, J.S. Convergence enhancement of super twisting sliding mode control using artificial neural network for DFIG based wind energy conversion systems. *IEEE Access* **2022**, *10*, 97625–97641. [CrossRef]

45. Mobayen, S.; Alattas, K.A.; Fekih, A.; El-Sousy, F.F.; Bakouri, M. Barrier function-based adaptive nonsingular sliding mode control of disturbed nonlinear systems: A linear matrix inequality approach. *Chaos Solitons Fractals* **2022**, *157*, 111918. [CrossRef]

46. Nguyen, A.; Lauber, J.; Dambrine, M. Optimal control based algorithms for energy management of automotive power systems with battery/supercapacitor storage devices. *Energy Convers. Manag.* **2014**, *87*, 410–420. [CrossRef]

47. Khalil, H.K. Lyapunov stability. *Control Syst. Robot. Autom.* **2009**, *12*, 115.